Measurement of bubble populations near the sea surface using combination frequencies: adaptation and calibration of device between two sea trials

A.D. Phelps and T.G. Leighton,
Institute of Sound and Vibration Research, University of Southampton, Southampton, UK, SO17 1BJ.

Abstract
This paper describes the application and calibration of a rig designed to employ a combination frequency technique to measure the size distribution of oceanic bubbles. Written between two sea trials, the paper describes how the apparatus was adapted for the specific oceanic environment, and describes the calibration process which allows the returned signal to be related to the size and number of resonant bubbles. It details how parameters such as the sensing volume and the contribution to the sound field by off-resonant bubbles were numerically estimated.

1. Introduction

There are many practical applications where a knowledge of the size and distribution of a bubble population would be of benefit [1-3], and the strong backscattering properties due to the impedance mismatch at the bubble surface make acoustic measurements particularly applicable. When excited by sound, bubbles pulsate volumetrically as a single degree of freedom system, where the inertia arises substantially from fluid around the bubble, the stiffness through gas compression inside the bubble, and the damping is brought on through viscous losses at the wall, thermal dissipation into the fluid and acoustic radiation. These volumetric pulsations have a well defined acoustic resonance frequency, given by [4]:

$$\omega_0 \approx \frac{1}{R_0\sqrt{\rho}}\sqrt{3\kappa\left(p_0+\frac{2\sigma}{R_0}\right)-\frac{2\sigma}{R_0}-\frac{4\mu^2}{\rho R_0^2}} \qquad (1)$$

where ω_0 is the resonant frequency in rad/s, R_0 is the equilibrium bubble radius, ρ is the density of the surrounding fluid (assumed to be incompressible), κ is the polytropic index of the gas, p_0 is the hydrostatic pressure at the bubble wall, σ is the surface tension of the gas / liquid interface and μ is the shear viscosity coefficient of the liquid.

Many of the limitations and ambiguities associated with monitoring both the linear and nonlinear single frequency backscatter from a bubble (for example, confusion between the signal scattered from a large bubble cloud and that from a single large bubble, poor spatial resolution, etc.) have been ameliorated through use of a two frequency technique [5]. A bubble population is simultaneously insonified with a high frequency fixed signal ω_i (the *imaging* signal) as well as a lower *pump* frequency signal ω_p intended to drive the population at their resonant frequencies [6]. When this low frequency sound field is coincident with a bubble resonance and the wall pulsations are large, the high frequency sound scattered from the bubble is amplitude modulated at this frequency, and this gives rise to sum-and-difference components in the returned signal at $\omega_i \pm \omega_p$. Therefore the technique allows the exploitation of the basic resonant behaviour of a bubble, but without the potential ambiguity caused when a large bubble is mistaken for a small resonant bubble. Additionally, the use of combination frequency measurements allows very specific spatial localisation, and the signal to noise ratio is greatly improved as the process translates only bubble-mediated information from the noisy frequency window around their resonance up to the comparatively quieter frequency window around the imaging signal.

This particular method of sizing bubbles has been investigated by earlier workers for laboratory populations employing increasingly more sophisticated signal processing techniques [6-8], and once on an oceanic population [9]. However, this latter work was performed over a very small pump frequency range (2.5 to 6 kHz), did not yield a measure of the absolute bubble number, and did not allow for some of the ambiguities and sources of error inherent in the technique itself and in the design of the apparatus, for example in the variable frequency response of the pump transducer. Recently, a more robust and accurate bubble population estimator was designed and built, and was used to successfully measure the bubble population in the surf zone at four discrete frequencies [10].

This paper details the calibration and design of an improved apparatus which employs two different measurement regimes to investigate the oceanic bubble population. The first uses ten discrete frequencies which span the expected range of resonances of bubbles found in the oceans. The second employs only two frequencies, and is intended to provide information on the time variant nature of the oceanic population. The text shows how potential ambiguities in the returned signal can be differentiated from the genuine bubble signals, and demonstrates how the substantial off-resonant contribution to the

$\omega_i \pm \omega_p$ signal can be allowed for in the calibration of the equipment. The paper first describes the theoretical model used in the estimation of the strength of the signal coupling, then proceeds to describe the calibration of the equipment. The experimental oceanic set-up is discussed, and preliminary laboratory measurements are presented which demonstrate the efficacy of the technique.

2. Calibration of the equipment

2.1. Analytical modelling techniques

Calibration of the measurement apparatus was performed to enable the energy of the $\omega_i \pm \omega_p$ signals to be related to the signal strength associated with one resonant bubble. This was achieved through examination of the acoustic scattering from a steady stream of bubbles of known size, and subsequently analytically modelling the expected signal. A comparison of the signal heights at the locations of the two combination frequency signals and the imaging signal between the modelled results and the experimental measurements allows the returned signal strength to be directly related to the number of resonant bubbles at that particular frequency.

The method used here produces absolute bubble counts, rather than relying on adjustable parameters or fitting models based on historical measurements to the data [11,12]. Earlier workers who analytically derived expressions for the height of the sum-and-difference terms [6,13] used simplified forms of the Rayleigh-Plesset equation to obtain expressions for the pressure amplitudes at the various frequency locations. However they took account only of viscous damping of the bubble motion, which is an order of magnitude smaller than damping through thermal and radiation losses (although it should be noted that Newhouse and Shankar [6] made the damping an unknown variable which they optimised to give best fit between their measured data and the bubble counts they expected). The algorithm for interpreting acoustic data in terms of bubble counts used in this paper uses a more accurate model of the bubble pulsation characteristics based on the formulations derived by Herring [14] and Keller [15], and can be written as:

$$\left(1-\frac{\dot{R}}{c}\right)R\ddot{R}+\frac{3}{2}\dot{R}^2\left(1-\frac{\dot{R}}{3c}\right)=\left(1+\frac{\dot{R}}{c}\right)\frac{1}{\rho}\left[p_B(t)-p_0-p\left(t+\frac{R}{c}\right)\right]+\frac{R}{\rho c}\frac{dp_B(t)}{dt} \quad (2)$$

where the symbols are defined earlier. Additionally, R is the instantaneous bubble radius, with its two derivatives with respect to time indicated with dots above the character, c is the speed of sound in

the fluid and $p(t)$ is the driving acoustic pressure. The remaining term $p_B(t)$ is a measure of the pressure immediately outside the bubble wall, and represents the forcing term on the liquid due to the bubble which the acoustic pressure has to overcome. It is given by:

$$p_B(t) = \left(p_0 + \frac{2\sigma}{R_0} \right) \left(\frac{R_0}{R} \right)^{3\kappa} - \frac{2\sigma}{R} - \frac{4\mu\dot{R}}{R} \tag{3}$$

Following the methodology presented by earlier workers [16,6], an approximate solution to this expression is sought by considering a small radial perturbation, where the variable R can be re-written in terms of a displacement variable x as:

$$R = R_0(1+x) \qquad \text{with} \quad x << 1 \tag{4}$$

Using this substitution, it is possible to re-write equations (2) and (3), where all terms beyond those in x^2 are neglected. The subsequent analysis involves writing a solution to the displacement variable x in terms of a sum of radial excursions at the six frequencies corresponding to ω_i, ω_p, $2\omega_i$, $2\omega_p$, $\omega_i + \omega_p$ and $\omega_i - \omega_p$, substituting this into the modified small amplitude Herring-Keller equation, and then equating the terms at the various different frequencies. The analytical solution is readily obtained (but cannot be simplified to obtain a transparent expression of the form obtained by earlier workers [6], and is therefore not presented here).

Because this greatly refined analysis includes for a finite speed of sound in the medium, rather than assuming the surrounding liquid to be incompressible, its explicitly allows for energy losses through acoustic radiation into the medium. By incorporating a polytropic relationship which relates the pressure of the gas inside the bubble to the radius, rather than the earlier assumed adiabatic relationship, the thermal damping losses are also considered. The value of κ is calculated theoretically using the expressions of Eller [17].

2.2. Laboratory measurements

The equipment schematic is shown in Fig. 1. To ensure that any potential signal corruption was identified and compensated for, the laboratory tests employed the apparatus exactly as it would later be used in the oceanic tests, and at the same anticipated depth for the transducers of 50 cm. The equipment hardware set-up is described elsewhere [10], although the deployment, control and calibration details differ (see below). The frequency response of the pump

transducer was previously calibrated over the frequency range employed in all the tests, allowing constant and known insonification conditions to be employed.

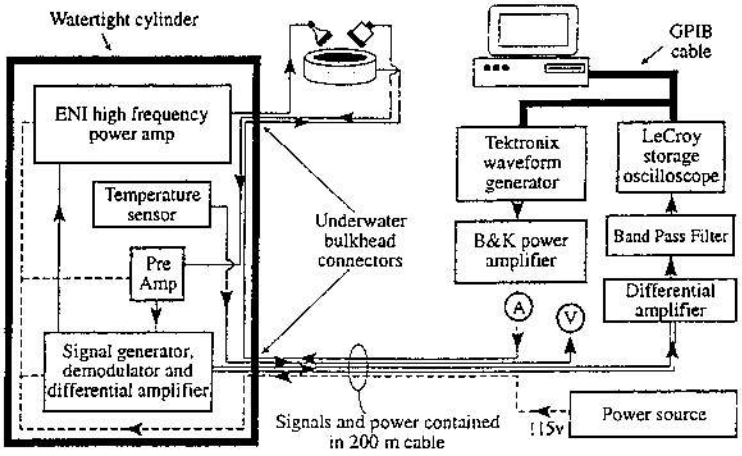

Fig. 1: Schematic of the apparatus used in both the laboratory and the oceanic measurements

The laboratory calibration on the stream was employed to both verify the model through comparison of its predictions with the measured energy distribution in the spectra scattered from the bubbles in the stream, and subsequently to estimate the sensitivity of the high frequency receiver transducer. Using this, and direct measurements of the frequency response of the preamplifier, demodulator, differential amplifiers and filters, allowed the measured signal strength to be directly related to the number of resonant bubbles within the transducer focus. The behaviour of bubbles resonant at the specific pump frequencies used in the oceanic tests could then modelled (using parameters applicable to sea water, rather than those of fresh water as used in modelling the lab tests). With application of the same sensitivity adjustment and the relevant preamplifier / demodulator / differential amplifier / filter corrections, this provided an estimate of the returned signal levels expected from bubbles resonant at the specific pump frequencies chosen. Using the same transducer geometry in the laboratory tests and the subsequent ocean trials allows certain parameters in the pulsation model to be poorly defined without any loss of accuracy [10].

The sensing volume was calculated by modelling the beam patterns of the two high frequency transducers by performing a Rayleigh integral over their surfaces. When these patterns were overlapped in the same layout as the transducer arrangement, they allowed the insonification volume to be estimated. This gave a volume,

defined by where the sensitivity fell off to 3 dB of its maximum value, of 1.0 cm^3. The result of such a procedure for the employed transducer geometry is shown in Fig. 2, where the distance between both the high frequency transducers and the focus is 16 cm and both transducers are angled at 45 ° to the vertically rising bubble flow.

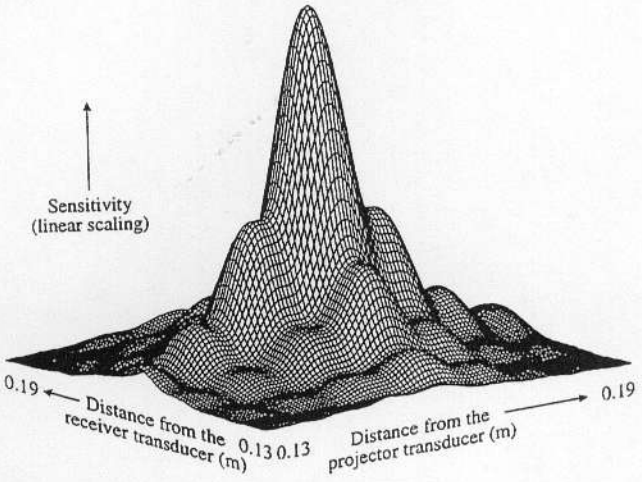

Fig. 2: The sensitivity within the sampling volume

The historical manner for presenting the bubble population information is as the number of bubbles at a particular bubble radius per cubic meter of water per micrometer radius range. Thus it is important to be able to determine the radius range over which the sum-and-difference signals persist, so this can be compensated for in the analysis. This was again achieved through the Herring-Keller simulations, where the radial width of each sum-and-difference peak was taken as the radius span before the signal height dropped by 3 dB.

2.3 Oceanic data collection

The most important difference in the proposed oceanic tests from the earlier surf zone measurements [10] is the intended deployment as a buoy in deep water. The high frequency generation and receiver equipment is housed in a remote equipment canister, again described elsewhere [10], and which will deployed in the sea and attached to the ship based equipment via an underwater bulkhead connector and 200 m of waterproof cable.

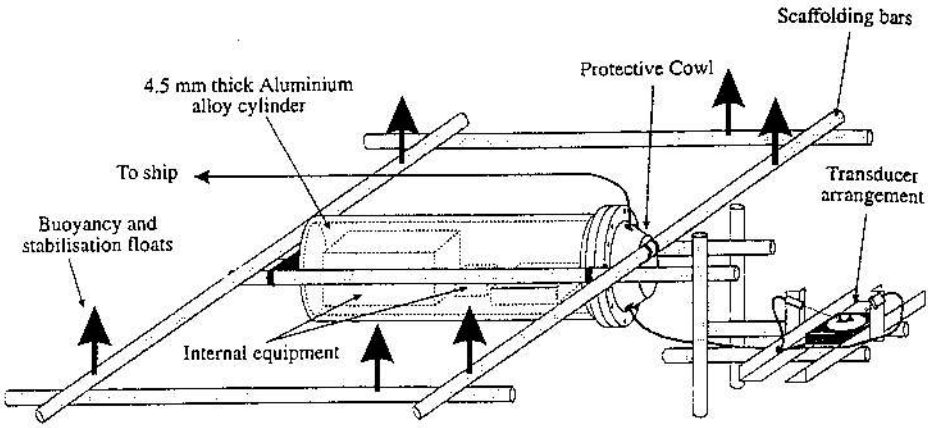

Fig. 3: Deployment details of the watertight canister and buoy

This paper is written just prior to tests in the deep ocean, for which the rig will employ two different pump signal regimes. In the first, pump frequencies of 17, 28, 50, 60, 88, 10, 145, 165, 180 and 200 kHz will be used, corresponding to bubble radii of 192, 116, 64, 53, 36, 29, 22, 19, 18 and 16 μm. These were chosen since examination of the results of earlier workers [11] indicated that, with bubble radius plotted on a logarithmic scale as is usual, these points would readily identify a possible peak in the spectrum at around $R \sim 20$ μm [11], whilst also indicating key gradients in the curve. The second regime will use fewer pump frequencies, enabling finer time resolution: the interval between consecutive tests using the ten pump frequencies in the first regime is 3 s, whilst in the second, where only two pump frequencies (17 and 145 kHz) are used, it is reduced to 0.85 s. Both regimes involve insonifying the bubble population at 1000 Pa in each frequency burst, with a time for each ten frequency snapshot of 0.1 s, and which is reduced to 0.02 s when employed in the second two frequency regime.

3. Results of laboratory tests

Fig. 4(a) shows a typical returned signal from the insonification of the laboratory bubble stream for a pump frequency of 4.8 kHz, and Fig 4(b) gathers the height of the imaging and the sum-and-difference peaks as the laboratory bubble stream was insonified through the bubbles' resonance frequency, between 3800 Hz and 5800 Hz in 25 Hz steps and with a pump amplitude of 200 Pa. The signal heights were found through FFTing the returned data, and then summing the energy over each peak. This was then converted back to a voltage measurement, as it was found that this gave the most accurate and

constant signal height estimates. The crosses shown above the three peaks in the figure indicate this equivalent signal voltage.

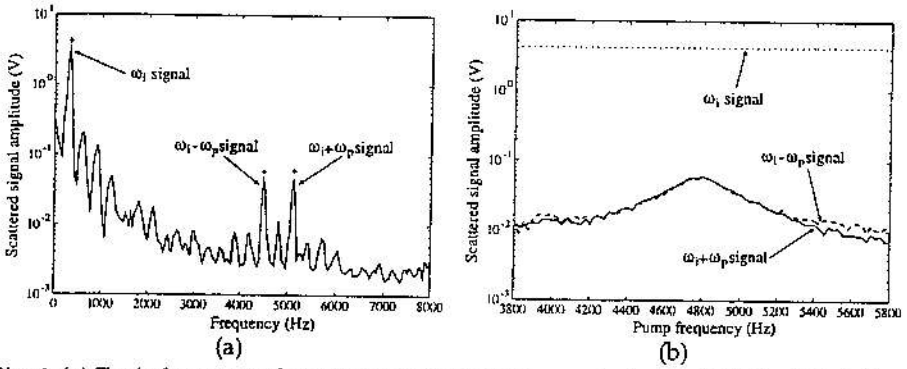

Fig. 4: (a) Typical spectrum from the laboratory measurements at ω_p = 4.8 kHz; (b) heights of the signals over the range of pump signals. The data was insonified between 2.8 and 5.8 kHz in 25 Hz steps, at an amplitude of 200 Pa. The crosses in (a) indicate the heights of the signals after the energy summation at each of the peaks.

The data in Fig. 4(a) shows the two $\omega_i + \omega_p$ and $\omega_i - \omega_p$ signals separated by approximately 600 Hz - this is evident because the scattered signals are subjected to a Doppler shift due to the bubble movement, and after demodulation the two peaks are shifted accordingly. The demodulated and Doppler shifted imaging signal is also evident at 300 Hz. The data in Fig. 4(a) shows the three signal heights over the entire range of pump signals. It is apparent that the bubbles in the stream are resonant at 4.8 kHz, with a returned signal height of 0.060 V at the location of the $\omega_i + \omega_p$ signal and 0.058 V at the $\omega_i - \omega_p$ signal. The imaging signal remains constant over the series of measurements, at a height of 4.15 V. This gives a ratio of the imaging signal to the $\omega_i + \omega_p$ signal of 36.8 dB and of 37.1 dB to the $\omega_i - \omega_p$ signal.

The second stage of the calibration involved modelling the bubble-mediated sound pressure at the receiver transducer due to the two insonifying sound fields signal. The same bubble size and insonification conditions as employed in the laboratory experiments were used, for a range of bubble sizes from 600 to 800 μm insonified by a 200 Pa amplitude sine wave of frequency 4800 Hz. The results from estimating the height of the two $\omega_i \pm \omega_p$ signals and the ω_i signal are shown in Fig. 5.

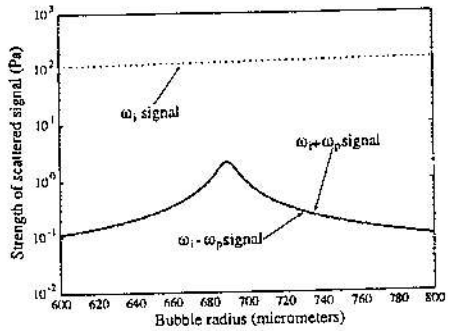

Fig. 5: Analytically derived amplitudes of the imaging, sum and difference signals for an insonifying sound field of frequency 4.8 kHz and amplitude of 200 Pa, over a radius range 600 - 800 μm.

It is clear from the figure that the strength of the $\omega_i + \omega_p$ and the $\omega_i - \omega_p$ signals reach a maximum of 2.13 Pa and 2.05 Pa respectively at a bubble radius of 689 μm, with a height of the scattered imaging signal of 129 Pa. The 3 dB width of the peak can also be estimated at 9.9 μm. This can be now compared with the measurements of the scattered signal from the 4800 Hz bubble stream. Comparison of the heights of the two imaging signal strengths, and consideration of the frequency responses of the preamplifier and demodulator, allow the sensitivity of the high frequency transducer to be estimated at 8.8 μV/Pa.

As a method of testing the validity of the model, the difference in the strengths of the imaging signal and the two sum-and-difference peaks were also calculated. The ratio of the imaging signal to the sum and difference terms is 35.7 dB and 36.0 dB respectively in the theoretical predictions, which results in a 1.1 dB discrepancy in both cases. This is equivalent to a 14 % error in the estimates of the sum and difference signal pressure. If the damping was taken to comprise viscous losses alone, and the thermal and radiation effects were to be ignored, the ratio of the two signal heights would be less than 1 dB, which is equivalent to a discrepancy of ~ 35 dB.

The output and data from the proposed ten frequency tests were partially verified in two subsequent tests. The first involved insonifying the calibration bubble stream of 689 μm radius bubbles with the ten frequency signal. Although the lowest frequency in the proposed range (17 kHz) is considerably higher than the bubbles' resonance (4.8 kHz), the returned data should still indicate the small presence of an off-resonant bubble. Additionally, any potential problems with the signal analysis should become evident in the process. The results are shown in Figs. 6(a) and (b).

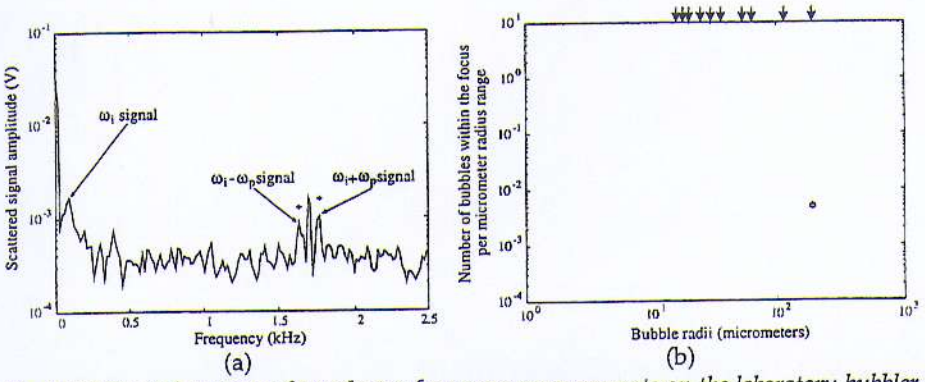

Fig. 6: (a) Typical spectrum from the ten frequency measurements on the laboratory bubbler, showing the Doppler shifted imaging signal and both the sum and difference peaks; (b) Estimates of the bubble population at the transducer focus. The data was insonified at an amplitude of 1000 Pa. The crosses in (a) indicate the heights of the signals after the energy summation at each of the peaks. In (b) the crosses indicate the bubble population estimate using the sum signal, and the circles using the difference signal.

Fig 6(a) shows the returned spectrum of the demodulated signal, again demonstrating the two frequency shifted sum-and-difference peaks. It should also be noted that the imaging signal is considerably smaller in magnitude from the earlier tests, caused by the inclusion of a 5 kHz high pass filter to remove the signal before acquisition, as it was found that this swamped the signal. Additionally, there is a second peak in between the sum-and-difference peaks at exactly 17 kHz. This is due in part to turbulence from the moving water causing a nonlinear coupling of the two sound fields, and also from the high frequency signal scattering from the transducer itself. It is clear that this non-bubble mediated signal can easily be identified and ignored during the analysis.

If the data is processed in the manner described earlier, a bubble number / size plot is obtained, as shown in Fig. 6(b). The plot shows the number of bubbles within the transducer focus per micrometer radius range, with the crosses showing the estimate calculated from using the $\omega_i + \omega_p$ signal and the circles showing the $\omega_i - \omega_p$ signal estimates. When no sum-and-difference signals were identifiable in the returned spectra as the signal heights were below the noise floor, the bubble count was assumed to be zero at that frequency, and thus these do not show on the logarithmic scale. The arrows at the top of the plot show the locations of the ten radii resonant with the pumping frequencies. It is clear that only one sum-and-difference peak was evident over the ten frequencies considered, and which showed the presence of $1/200^{th}$ of a resonant bubble for both signals. The implications of this will be discussed in the next section.

Following on from the measurements on the simple bubbler, the air flow to the needle was increased. This had the effect of introducing a population of much smaller bubbles as well as increasing the rate of production of the larger ~ 700 μm bubbles (although their exact size was not re-measured directly). The results from a ten frequency measurement on the faster stream are shown in Fig. 7.

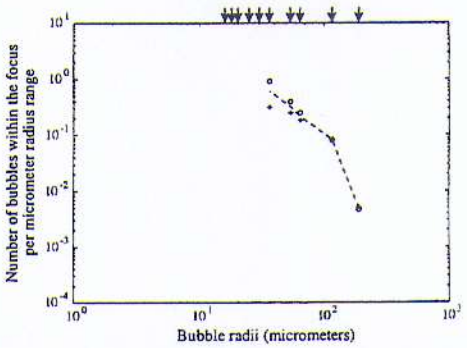

Fig. 7: Estimates of the bubble population at the transducer focus using the laboratory bubbler with an increased air flow. The data was insonified at an amplitude of 1000 Pa. The crosses indicate the bubble population estimate using the sum signal, and the circles using the difference signal, with the average indicated with the dashed line.

It is apparent from this data that the bubbler was producing an additional stream of bubbles of radii between 35 and 120 μm. As the bubbles became smaller, there appears to be an increasing divergence between the estimate of the bubble numbers from the sum and the difference signals. The dotted line shows the average of the two, and the implications of this effect are discussed below. Again, if no sum-and-difference peaks were identifiable in the spectra, the bubble count was set to zero at that pump frequency.

4. Discussion

Although there is no ground truthing for the measurements on the bubble stream using the ten frequency population estimates, the data confirms that the sum-and-difference signals are suitably identifiable in the returned signals to allow it to potentially be a useful bubble measurement technique. Additionally, the estimates of the population examine the height of the $\omega_i - \omega_p$ signals as well as the $\omega_i + \omega_p$ signal, as was previously performed [10]. For the larger bubble sizes, the estimates for the population seem to agree very well using the two signals, but as the bubbles become smaller, the two estimates diverge. This is probably a manifestation of truncating the expanded Herring Keller formulation at only terms up to x^2. It is likely that the $\omega_i - \omega_p$

estimates of the population are too high, and the $\omega_i + \omega_p$ estimates are correspondingly low, and thus averaging the two would yield a more accurate measure.

The appearance of the bubble signal at 17 kHz from a 4.8 kHz bubble can be further investigated. If the analytical height of the resonant peak for a bubble at 17 kHz is plotted, as shown in Fig. 8, it is evident that the signal peaks at a bubble radius of 192 μm with an $\omega_i + \omega_p$ signal height of 3.1 Pa. If the curve is extended to encompass larger bubbles to examine their off-resonant contribution to the sum-and-difference scattering at 17 kHz, it is apparent that a 689 μm bubble (such as those produced by the bubbler resonant at 4.8 kHz) scatters a signal of height 0.014 Pa. This is 1 / 220th of the scattered pressure of the resonant bubble, and so would appear as 1 / 220th of a resonant bubble in the population estimates. This is very close to the actual measure shown in Fig. 6(b).

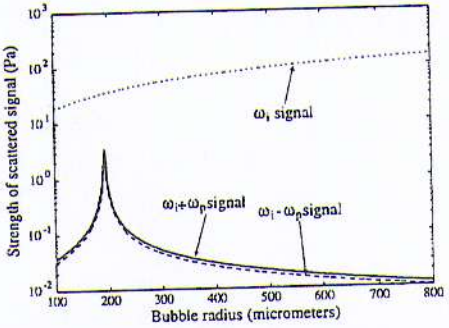

Fig. 8: Analytically derived amplitudes of the imaging, sum and difference signals for an insonifying sound field of 17 kHz and amplitude 1000 Pa, over an extended radius range of 100 to 800 μm.

5. Conclusions

This paper demonstrated how a combination-frequency technique can be employed to measure the oceanic bubble population. The returned signals are calibrated to give absolute bubble counts, through a comparison of laboratory measurements and analytically derived signal heights based on the Herring-Keller model. The latest oceanic rig employs ten pump frequencies designed to measure the population between 16 and 192 μm in two regimes, designed to yield information on the bubble population and its time variance. Preliminary results taken using a bubble in the laboratory have demonstrated the potential for this measurement technique and calibration procedure, and it is envisaged that oceanic data will be collected in the very near future.

Acknowledgements

The authors wish to acknowledge the Natural Environment Research Council (grant GR3 09992) for support, and A. Hall for assistance with the design of the bubble measurement buoy.

References

1. Thorpe, S., On the clouds of bubbles formed by breaking wind-waves in deep water, and their role in air-sea gas transfer. *Philos. Trans. R. Soc. London*, 1982, **A304**, 155-210.
2. Belcher, E.O., Quantification of bubbles formed in animals and man during decompression. *IEEE Trans. Biomed. Eng.*, 1980, 27, 330-338.
3. Tickner, E.G., Precision microbubbles for right side intercardiac pressure and flow measurements. In *Contrast Echocardiography*, ed. R.S. Meltzer and J. Roeland, Nijhoff, London, 1982.
4. Leighton, T.G., *The Acoustic Bubble*, Academic Press, London, 1994.
5. Leighton, T.G., Ramble, D.G. and Phelps, A.D., The detection of tethered and rising bubbles using multiple acoustic techniques. *J. Acoust. Soc. Am.*, (In press).
6. Newhouse, V.L. and Shankar, P.M., Bubble sizing using the nonlinear mixing of two frequencies. *J. Acoust. Soc. Am.*, 1984, **75**, 1473-1477.
7. Chapelon, J.Y., Shankar, P.M. and Newhouse, V.L., Ultrasonic measurement of bubble cloud size profiles. *J. Acoust. Soc. Am.*, 1985, **78**, 196-201.
8. Shankar, P.M., Chapelon, J.Y. and Newhouse, V.L., Fluid pressure measurement using bubbles insonified by two frequencies. *Ultrasonics*, 1986, **24**, 333-336
9. Koller, D., Li, Y., Shankar, P.M. and Newhouse, V.L., High speed bubble sizing using the double frequency technique for oceanographic applications. *IEEE J. Oceanic Eng.*, 1992, **17**, 288-291.
10. Phelps, A.D., Ramble, D.G. and Leighton, T.G., The use of a combination frequency technique to measure the surf zone bubble population. *J. Acoust. Soc. Am.*, 1997, **101**, 1981-1989.
11. Farmer, D.M. and Vagle, S., Waveguide propagation of ambient sound in the ocean-surface bubble layer. *J. Acoust. Soc. Am.*, 1989, **86**, 1897-1908.
12. Breitz, N. and Medwin, H., Instrumentation for in situ acoustical measurements of bubble spectra under breaking waves. *J. Acoust. Soc. Am.*, 1989, **86**, 739-743.
13. Zabolotskaya, E.A. and Soluyan, S.I., Emission of harmonic and combination-frequency waves by air bubbles. *Sov. Phys. Acoust.*, 1973, **18**, 396-398.
14. Herring, C., Theory of the pulsations of the gas bubble produced by an underwater explosion. Report No. 236, OSRD, 1941.
15. Keller, J.B and Miksis, M., Bubble oscillations of large amplitude, *J. Acoust. Soc. Am.*, 1980, **68**, 628-633.
16. Miller, D.L., Ultrasonic detection of resonant cavitation bubbles in a flow tube by their second- harmonic emissions. *Ultrasonics*, 1981, **19**, 217-224
17. Eller, A.I., Damping constants of pulsating bubbles. *J. Acoust. Soc. Am.*, 1970, **47**, 1469-1470